Computers and Mathematics with Applications 125 (2022) 25–33

Contents lists available at ScienceDirect

Computers and Mathematics with Applications

www.elsevier.com/locate/camwa

Phase-field computations of anisotropic ice crystal growth on a spherical surface

Chaeyoung Lee [a], Sungha Yoon [b], Jintae Park [a], Hyundong Kim [c], Yibao Li [d], Darae Jeong [e], Sangkwon Kim [a], Soobin Kwak [a], Junseok Kim [a,*]

[a] *Department of Mathematics, Korea University, Seoul 03760, Republic of Korea*
[b] *Institute of Mathematical Sciences, Ewha Womans University, Seoul 30019, Republic of Korea*
[c] *Institute for the Advanced Study of Human Biology (WPI-ASHBi), Kyoto University Institute for Advanced Study, Kyoto University, Kyoto 6068501, Japan*
[d] *School of Mathematics and Statistics, Xi'an Jiaotong University, Xi'an 710049, China*
[e] *Department of Mathematics, Kangwon National University, Gangwon-do 24341, Republic of Korea*

ARTICLE INFO

Keywords:
Ice crystal growth
Phase-field model
Spherical surface

ABSTRACT

In this paper, we present a numerical method for the phase-field model of anisotropic ice crystal growth on a spherical surface. The mathematical model includes terms related to the anisotropic interfacial energy, which is defined by the interface angle with respect to a reference angle. One of the natural numerical methods on curved surfaces is a computational technique based on a triangular mesh for the surface in a three-dimensional space. However, it is difficult to compute terms with the interface angle on a triangular mesh. To resolve this problem, we solve the governing equation in Cartesian coordinates after rotating each vertex and the 1-ring neighborhood of the vertex on the triangular mesh. After rotation and interpolation, we numerically solve the phase-field model using a standard finite difference method. We present the results of several tests to demonstrate that the proposed algorithm can recover anisotropic ice crystal growth on a spherical surface.

1. Introduction

In this study, it is demonstrated that a computational method for the phase-field model of anisotropic ice crystal growth on a spherical surface. Figs. 1(a) and (b) present snapshots of the freezing of a bubble that is stacked on an icy substrate after 1 and 3 seconds, respectively [1], wherein freezing dynamics of soap bubbles are characterized using experiments, scaling analysis, and computational techniques. In addition, an online search for the term "frozen bubbles" reveals a lot of beautiful and mesmerizing photographs and videos of the freezing of soap bubbles. Significantly small particles of freezing ice move around on the surface of a soap bubble until they grow and occupy the entire surface.

The mechanisms of the freezing phenomenon have been studied both theoretically and experimentally [2–5]. Based on these investigations, there have been numerous studies on computational simulations of crystal growth. Langer [6] and Kobayashi [7] developed a phase-field model for solidification, including the relations between anisotropy and the shape of crystals. In [8], Karma and Rappel simulated dendritic growth in two- and three-dimensional spaces using the phase-field model. Employing the above phase-field models with anisotropic interface, researchers have studied two specific features of ice crystal growth: the faceted growth and the strong aspect ratio of ice crystals [9–11]. In the references, the authors considered both highly anisotropic surface energy and kinetic effects, and validated the side branching. In [9], Barret et al. proposed the unconditionally stable approximation for the Stefan problem using a finite element method. Demange et al. [10,11] reproduced a host of three-dimensional snowflake morphologies with both planar and vertical growth morphologies using a faceted phase-field model derived from Karma and Rappel's seminal work and Eggleston's regularization algorithm with anisotropic interface.

Recently, several researchers have proposed numerical methods to obtain better results for the dendrite growth during solidification. In [12], Sun et al. adopted lattice Boltzmann method based on cellular automaton approach to simulate the equiaxed crystal growth. Meng et al. [13] combined the lattice Boltzmann and immersed boundary methods to improve the accuracy of dendrite pattern generation against

---

* Corresponding author.
E-mail address: cfdkim@korea.ac.kr (J. Kim).
URL: http://math.korea.ac.kr/~cfdkim (J. Kim).

https://doi.org/10.1016/j.camwa.2022.08.035
Received 26 October 2021; Received in revised form 13 June 2022; Accepted 23 August 2022

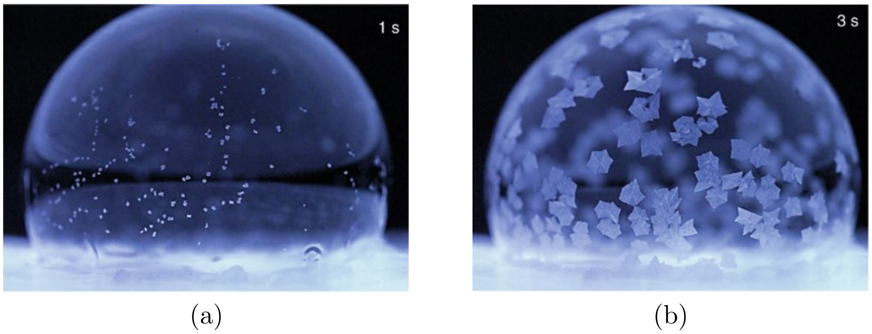

(a) (b)

Fig. 1. Freezing of a bubble stacked on an icy substrate: after (a) 1 second and (b) 3 seconds. Reprinted from Ahmadi et al. [1] with permission from Nature Publishing Group.

advection. In particular, accuracy is typically important because the collision and coalescence of dendrite patterns occur during the simulation of multiple moving dendrites. Tan et al. [14] developed and demonstrated the ice crystal growth based on the lattice Boltzmann method. They studied the branches with a faceted structure following the symmetry of the crystal and modeled the ice crystal growth in a two-dimensional domain in presence of convection. Ren et al. [15] proposed a vector-valued phase-field and two-phase flow model, which facilitated a flow field evaluation with a steep viscosity variation across the interface. The authors presented a parallel multilevel time marching scheme. Moreover, mathematical models for dendritic growth with fluid flow have been proposed [16–18]. However, these approaches involve a high computational cost when conducting numerical experiments in a three-dimensional space or when the flow fields are coupled. Various numerical methods have been proposed to facilitate more efficient computation [19–21]. In [19], the authors proposed an adaptive mesh approach for simulating the solidification of microstructures in two- and three-dimensional spaces. In [20], an accurate and fast adaptive algorithm for dendritic growth was developed without a conventional adaptive structure. Chen and Yang [21] proposed an unconditionally energy stable numerical scheme for solving a nonlinear system that represents anisotropic dendritic growth.

Ice crystal formulations are also observed on curved surfaces and not only in two- or three-dimensional spaces. The authors in [22] investigated colloidal crystals growing on spherical droplets. They examined that the formation of regions with branched patterns and large voids, avoiding topological defects. It was demonstrated that curvature-induced elastic energy was minimized by this morphology. Topological defect nucleation and boundary branching in crystal growth are examples of instabilities caused by curvature-induced stress. Therefore, the elucidation of their mechanisms is highly relevant. Ma et al. [23] studied the interaction between dislocation nucleation and boundary instability on curved surfaces during crystal growth and demonstrated the growth of curved crystals using Brownian dynamics simulations. In [24], a two-dimensional dendritic growth simulation on curved surfaces was performed in spherical coordinates using a phase-field model. The effect of the curvature of spheres on the growth of a crystal was investigated. In [25], the authors presented the results of a computational simulation of isotropic crystal growth on curved surfaces in a three-dimensional space. As global warming progresses, research on the growth of ice in the sea is also becoming more prevalent. Tang [26] proposed sea ice growth modeling using the phase-field method and stated a long time behavior weak solution. To the best of our knowledge, there are few computational simulations of anisotropic crystal growth on curved surfaces using the phase-field model.

For anisotropic ice crystal growth on spherical surfaces, a phenomenological total free energy is considered in a two-dimensional space as follows [8,27–30]:

$$\mathcal{F} = \int \left[\frac{\epsilon^2(\theta)}{2} |\nabla \phi|^2 - \frac{\phi^2}{2} + \frac{\phi^4}{4} + \lambda U \left(\phi - \frac{2\phi^3}{3} + \frac{\phi^5}{5} \right) \right] d\mathbf{x}, \tag{1}$$

where ϕ is the order parameter [31], λ is a positive parameter, U is the dimensionless temperature, and the anisotropic term is

$$\epsilon(\theta) = \epsilon_0 (1 + \epsilon_6 \cos(6\theta)). \tag{2}$$

Here, ϵ_0 and ϵ_6 are interfacial parameters, and θ is the angle between the normal vector, $-\nabla\phi = (-\phi_x, -\phi_y)$, of the interface and the x-axis, i.e., $\theta = \tan^{-1}\left(\phi_y/\phi_x\right)$. Thus, the governing equation for anisotropic ice crystal growth can be derived using a variational approach:

$$\epsilon^2(\theta) \frac{\partial \phi}{\partial t} = -\frac{\delta \mathcal{F}}{\delta \phi}, \tag{3}$$

i.e.,

$$\begin{aligned} \epsilon^2(\theta) \frac{\partial \phi}{\partial t} &= \nabla \cdot (\epsilon^2(\theta) \nabla \phi) + [\phi - \lambda U (1 - \phi^2)](1 - \phi^2) \\ &\quad + \left(|\nabla \phi|^2 \epsilon(\theta) \frac{\partial \epsilon(\theta)}{\partial \phi_x} \right)_x + \left(|\nabla \phi|^2 \epsilon(\theta) \frac{\partial \epsilon(\theta)}{\partial \phi_y} \right)_y, \end{aligned} \tag{4}$$

$$\frac{\partial U}{\partial t} = D \Delta U + \frac{1}{2} \frac{\partial \phi}{\partial t}, \tag{5}$$

where D is the thermal diffusivity. The following terms can be simplified to Eq. (4):

$$\begin{aligned} \left(|\nabla \phi|^2 \epsilon(\theta) \frac{\partial \epsilon(\theta)}{\partial \phi_x} \right)_x &= \left((\phi_x^2 + \phi_y^2) \epsilon(\theta) \epsilon'(\theta) \left(-\frac{\phi_y}{\phi_x^2 + \phi_y^2} \right) \right)_x \\ &= -\left(\epsilon'(\theta) \epsilon(\theta) \phi_y \right)_x, \\ \left(|\nabla \phi|^2 \epsilon(\theta) \frac{\partial \epsilon(\theta)}{\partial \phi_y} \right)_y &= \left((\phi_x^2 + \phi_y^2) \epsilon(\theta) \epsilon'(\theta) \frac{\phi_x}{\phi_x^2 + \phi_y^2} \right)_y = \left(\epsilon'(\theta) \epsilon(\theta) \phi_x \right)_y. \end{aligned}$$

Therefore, Eqs. (4) and (5) can be rewritten as

$$\begin{aligned} \epsilon^2(\theta) \frac{\partial \phi}{\partial t} &= \nabla \cdot (\epsilon^2(\theta) \nabla \phi) + [\phi - \lambda U (1 - \phi^2)](1 - \phi^2) \\ &\quad - \left(\epsilon'(\theta) \epsilon(\theta) \phi_y \right)_x + \left(\epsilon'(\theta) \epsilon(\theta) \phi_x \right)_y, \end{aligned} \tag{6}$$

$$\frac{\partial U}{\partial t} = D \Delta U + \frac{1}{2} \frac{\partial \phi}{\partial t}. \tag{7}$$

It becomes very complicated and difficult to implement numerical simulations on curved surfaces [33,34]. One of natural computational methods on curved surfaces is to solve the governing equations on a triangular mesh for the surface in a three-dimensional space [32]. However, it is difficult to compute the terms $\epsilon(\theta)$ in Eq. (6) with interface angle on the triangular mesh.

The main purpose of this paper is to resolve this problem by solving the governing equation in Cartesian coordinates after rotating each vertex and the 1-ring neighborhood of the vertex on the triangular mesh. After rotation and interpolation, the governing equation is numerically solved by applying a standard finite difference scheme.

The remainder of this paper is organized as follows. In Section 2, the numerical solution algorithm is described in detail. In Section 3, various tests are performed to demonstrate that the proposed algorithm can

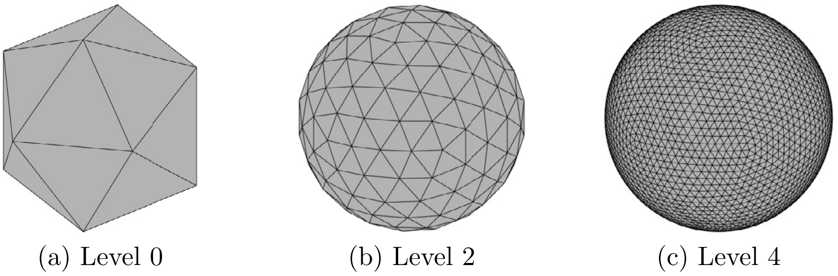
(a) Level 0　(b) Level 2　(c) Level 4

Fig. 2. Triangular surface meshes with different levels. The refinement level is described in each figure.

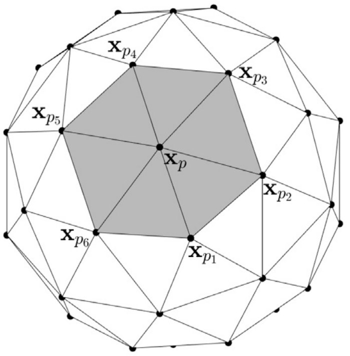

Fig. 3. Schematic of the triangular surface mesh and 1-ring neighbors of $\mathbf{x}_p$.

recover anisotropic ice crystal growth on a spherical surface. In Section 4, we discuss the numerical methods and results, and present the strengths and weaknesses of the proposed method. Finally, conclusions are summarized in Section 5.

2. Numerical solution algorithm

In this section, a numerical method is proposed for the phase-field model of anisotropic ice crystal growth on a spherical surface. Let us consider a sphere of radius R centered at $(x, y, z) = (0, 0, 0)$. A triangular mesh of the spherical surface $\mathcal{S}$ is generated by adopting the SphereMesh function in MATLAB [35]. Starting from the icosahedron (level 0), as shown in Fig. 2(a), to define higher-level surface meshes, the triangles are recursively refined by connecting the midpoints of each side and scale the newly generated points such that they lie on the surface of the sphere. Fig. 2(b) and (c) show the generated triangular surface meshes with level 2 and 4, respectively.

Given the spherical surface $\mathcal{S}$, we first define a triangular surface mesh $\mathcal{M}$ with a set of M vertices, i.e., $\mathcal{M} = \{\mathbf{x}_p\}_{p=1}^{M}$. Fig. 3 illustrates the 1-ring neighborhood of a vertex $\mathbf{x}_p$, i.e., $\{p_1, p_2, \cdots, p_q\}$ which are connected to $\mathbf{x}_p$ by an edge. In this mesh generation, $q = 5$ or $q = 6$.

Now, we describe the numerical solution algorithm in detail. For $p = 1, \ldots, M$, let $\mathbf{m}$ be the unit vector that is perpendicular to both $\mathbf{x}_p$ and $(0, 0, R)$ as the normalized cross product of the two vectors (see Fig. 4(a)), i.e.,

$$\mathbf{m} = \frac{\mathbf{x}_p \times (0, 0, R)}{|\mathbf{x}_p \times (0, 0, R)|}. \tag{8}$$

Let φ be the angle between the two vectors $\mathbf{x}_p$ and $(0, 0, R)$ (see Fig. 4(a)), i.e.,

$$\varphi = \cos^{-1}\left(\frac{\mathbf{x}_p \cdot (0, 0, R)}{|\mathbf{x}_p||(0, 0, R)|}\right). \tag{9}$$

The 1-ring neighborhood is rotated about the unit vector $\mathbf{m}$ by an angle φ using the following formula [36]:

$$\tilde{\mathbf{x}}_{p_i} = (1 - \cos(\varphi))(\mathbf{x}_{p_i} \cdot \mathbf{m})\mathbf{m} + \cos(\varphi)\mathbf{x}_{p_i} + \sin(\varphi)\mathbf{m} \times \mathbf{x}_{p_i}, \ i = 1, \ldots, q. \tag{10}$$

In addition, the center point $\mathbf{x}_p$ of the 1-ring neighborhood moves to the north pole $\tilde{\mathbf{x}}_p = (0, 0, R)$, as shown in Fig. 4(a).

Then, the 1-ring transferred points $\tilde{\mathbf{x}}_{p_i}$ are projected onto the xy-plane and let the corresponding projected points be $\hat{\mathbf{x}}_{p_i}$. Through this process, the original arc-length connecting $\tilde{\mathbf{x}}_{p_i}$ and $(0, 0, R)$ is changed. As shown in Fig. 4(b), the arc-length is recovered by scaling and define $\bar{\mathbf{x}}_{p_i}$ as

$$\bar{\mathbf{x}}_{p_i} = R\cos^{-1}\left(\frac{\tilde{\mathbf{x}}_{p_i} \cdot (0, 0, R)}{|\tilde{\mathbf{x}}_{p_i}||(0, 0, R)|}\right)\frac{\hat{\mathbf{x}}_{p_i}}{|\hat{\mathbf{x}}_{p_i}|}. \tag{11}$$

Next, let h_p be the radius of the inscribed circle of the polygon consisting of projected points for $p = 1, \ldots, M$ and then let h_{min} be the minimum of the radii h_p, i.e., $h_{min} = \min_{1 \le p \le M} h_p$. A local space step h is defined as $h = sh_{min}$, where $0 < s \le 1/\sqrt{2}$ is a safety scaling factor. We then interpolate the phase-field values s_i $(i = 1, \ldots, 17)$ and the temperature field values V_i $(i = 1, \ldots, 9)$ from the projected values using the scatteredInterpolant function in MATLAB [37].

Let $\phi_p^n = \phi(x_p, y_p, z_p, n\Delta t)$ and $U_p^n = U(x_p, y_p, z_p, n\Delta t)$, where Δt is the time step size. Then, using an explicit Euler scheme, the governing equations (6)–(7) are discretized as follows:

$$\begin{aligned}\epsilon^2(\theta_p^n)\frac{\phi_p^{n+1} - \phi_p^n}{\Delta t} &= \left[\nabla_d \cdot (\epsilon^2(\theta)\nabla_d \phi)\right]_p^n + [\phi_p^n - \lambda U_p^n(1 - (\phi_p^n)^2)][1 - (\phi_p^n)^2] \\ &\quad - \left[D_x\left(\epsilon'(\theta)\epsilon(\theta)D_y\phi\right)\right]_p^n + \left[D_y\left(\epsilon'(\theta)\epsilon(\theta)D_x\phi\right)\right]_p^n, \end{aligned} \tag{12}$$

$$\frac{U_p^{n+1} - U_p^n}{\Delta t} = D\Delta_d U_p^n + \frac{\phi_p^{n+1} - \phi_p^n}{2\Delta t}, \tag{13}$$

where θ_p is the angle at $\mathbf{x}_p$, and $\nabla_d \phi = (D_x\phi, \ D_y\phi)$ is the discrete gradient. The explicit Euler scheme has a limitation on the time step size, however, it is not a severe constraint because the governing equation is a second-order partial differential equation. Moreover, even with an implicit Euler scheme applied, small time step sizes should be used to obtain an accurate solution [20,38]. Equations (12) and (13) are solved by using the two-dimensional Cartesian local coordinate values s_i and V_i, as illustrated in Fig. 4(c) and (d). For simplicity of exposition, the superscript n is omitted. In Eq. (12), the anisotropic function and its derivative are as follows:

$$\epsilon(\theta_p) = \epsilon_0\left(1 + \epsilon_6\cos(6(\theta_p - \bar{\theta}))\right), \tag{14}$$

$$\epsilon'(\theta_p) = -6\epsilon_0\epsilon_6\sin(6(\theta_p - \bar{\theta})), \tag{15}$$

where $\bar{\theta}$ is the orientation angle. In this paper, $\bar{\theta} = \pi/6$ is used because we consider a small square in a regular hexagon that consists of six regular triangles with an angle of $\pi/3$. To compute $\epsilon^2(\theta_p)$, the outward normal vector of the interface at $(0, 0)$ in the local coordinate is defined as shown in Fig. 4(c):

$$-\nabla_d\phi_p = -\left(\frac{s_{14} - s_{13}}{h}, \ \frac{s_{16} - s_{11}}{h}\right). \tag{16}$$

Then, the angle between the normal vector and a reference axis $(1, 0)$ is given as

$$\theta_p = \tan^{-1}\left(\frac{s_{11} - s_{16}}{s_{13} - s_{14}}\right). \tag{17}$$

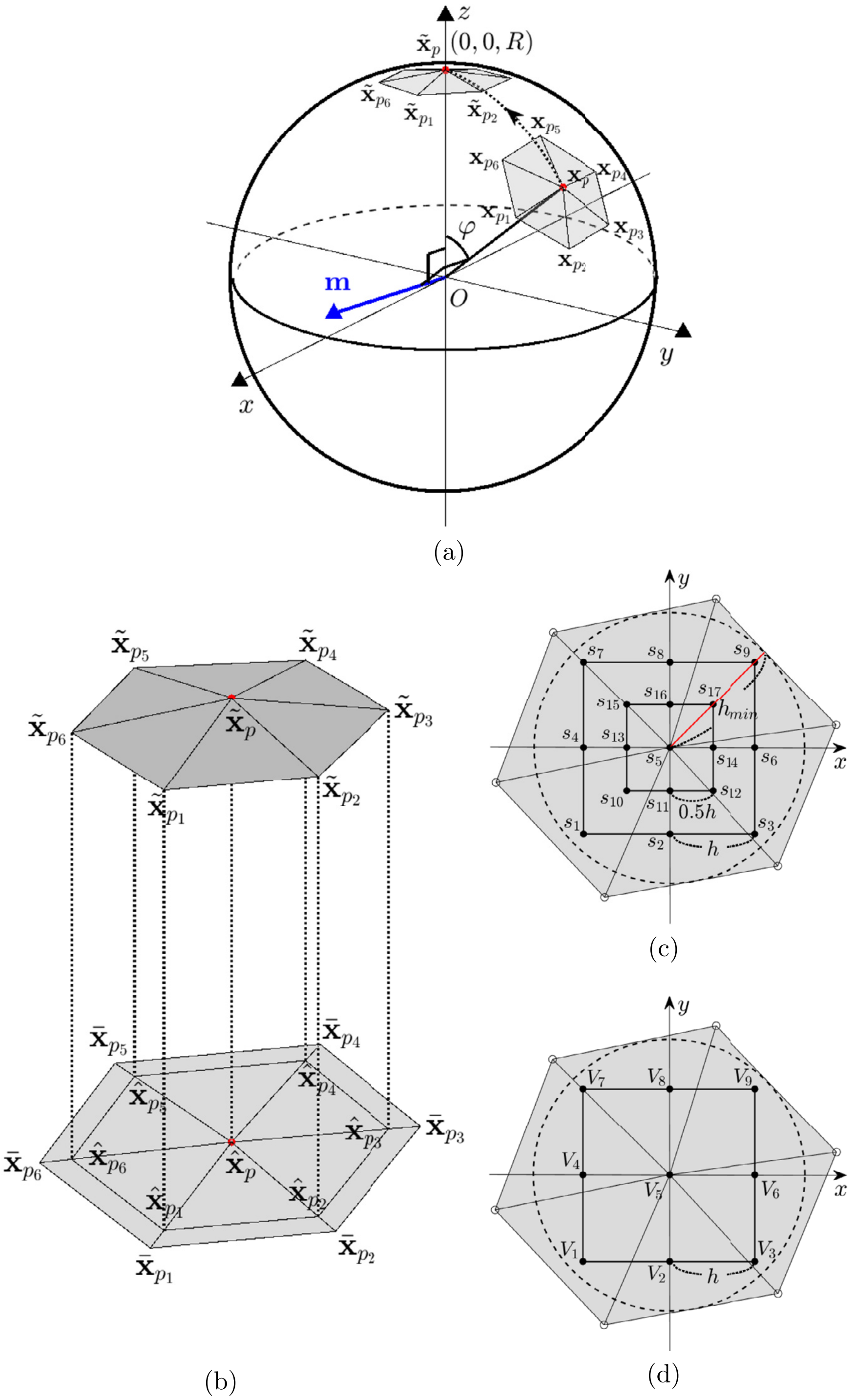

Fig. 4. Schematic of moving points of the 1-ring and normal vector **m**: (a) three-dimensional view and (b) projection of the 1-ring and normalization. Schematic of the two-dimensional Cartesian local coordinates for solving the governing equations: (c) 17 points s_i $(i = 1, 2, \dots, 17)$ in the 1-ring for the phase-field values, and (d) 9 points V_i $(i = 1, 2, \dots, 9)$ in the 1-ring for the temperature field values.

Using this angle θ_p and Eq. (14), $\epsilon^2(\theta_p)$ is computed. Next, let us define the discretization of the other terms as follows:

$$\left[\nabla_d \cdot (\epsilon^2(\theta)\nabla_d \phi)\right]_p = \frac{\epsilon^2(\theta_{\frac{1}{2},0})\left(s_6 - s_5\right) - \epsilon^2(\theta_{-\frac{1}{2},0})\left(s_5 - s_4\right)}{h^2} + \frac{\epsilon^2(\theta_{0,\frac{1}{2}})\left(s_8 - s_5\right) - \epsilon^2(\theta_{0,-\frac{1}{2}})\left(s_5 - s_2\right)}{h^2},$$

$$\left[D_x\left(\epsilon'(\theta)\epsilon(\theta)D_y\phi\right)\right]_p = \frac{\epsilon'(\theta_{\frac{1}{2},0})\epsilon(\theta_{\frac{1}{2},0})\left(s_{17} - s_{12}\right) - \epsilon'(\theta_{-\frac{1}{2},0})\epsilon(\theta_{-\frac{1}{2},0})\left(s_{15} - s_{10}\right)}{h^2},$$

$$\left[D_y\left(\epsilon'(\theta)\epsilon(\theta)D_x\phi\right)\right]_p = \frac{\epsilon'(\theta_{0,\frac{1}{2}})\epsilon(\theta_{0,\frac{1}{2}})\left(s_{17} - s_{15}\right) - \epsilon'(\theta_{0,-\frac{1}{2}})\epsilon(\theta_{0,-\frac{1}{2}})\left(s_{12} - s_{10}\right)}{h^2},$$

where $\theta_{i,j}$ is the angle between the normal vector of the interface and $(1,0)$ at a point (hi, hj), i.e.,

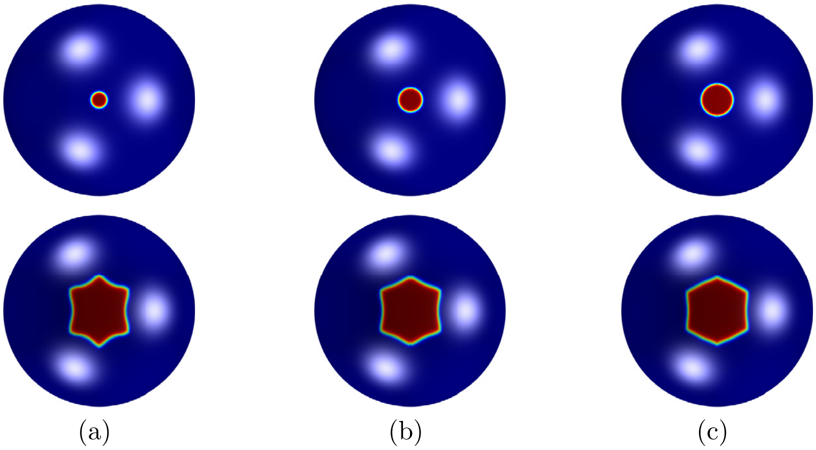

Fig. 5. Crystal growth on a sphere with different initial radii R_0 at (a) $t = 1200\Delta t$, (b) $t = 1000\Delta t$, and (c) $t = 800\Delta t$. From left to right, $r = 10, 15$ and 20.

$$\theta_{-\frac{1}{2},0} = \tan^{-1}\left(\frac{s_{10} - s_{15}}{s_4 - s_5}\right),\ \theta_{\frac{1}{2},0} = \tan^{-1}\left(\frac{s_{12} - s_{17}}{s_5 - s_6}\right), \tag{18}$$

$$\theta_{0,-\frac{1}{2}} = \tan^{-1}\left(\frac{s_2 - s_5}{s_{10} - s_{12}}\right),\ \theta_{0,\frac{1}{2}} = \tan^{-1}\left(\frac{s_5 - s_8}{s_{15} - s_{17}}\right). \tag{19}$$

Finally, the discretization of the Laplacian operator [39] for temperature is

$$\Delta_d U_p = \frac{4(V_2 + V_4 + V_6 + V_8) + V_1 + V_3 + V_7 + V_9 - 20V_5}{6h^2}. \tag{20}$$

A brief summary of the algorithm presented in this section is as follows: We first move the object which we need to compute on the sphere such as the hexagonal part shown in Fig. 4(a) toward the north pole; project it on the two-dimensional plane as shown in Fig. 4(b) and create the square mesh grid on the flat domain as shown in Fig. 4(c), keeping the distance between the center point and other points fixed and expanding other inter-point distances as necessary; and then interpolate the phase-field values as shown in Fig. 4(d). We finally solve the discrete governing equations (12)–(13).

3. Numerical results

In this section, various numerical experiments are performed to demonstrate the efficiency of the proposed scheme on spherical surfaces in a three-dimensional space. Unless otherwise indicated, for triangular surface meshes with level 6 and a spherical radius $R = 120$, the following parameters are used: $\lambda = 3.1913, \epsilon_0 = 1,\ \epsilon_6 = 0.05,\ s = 0.5/\sqrt{2},\ D = 1$, and $\Delta t = 0.1h^2/D$. The initial condition is set to, for $p = 1, \dots, M$,

$$\begin{aligned} \phi(x_p, y_p, z_p, 0) &= \tanh\left(\frac{r - R\theta}{0.01\sqrt{2}R}\right), \\ U(x_p, y_p, z_p, 0) &= \frac{1 - \phi(x_p, y_p, z_p, 0)}{2}\Delta, \end{aligned} \tag{21}$$

where $\theta = \cos^{-1}\left((x_p, y_p, z_p) \cdot (0, 0, R)\right)$, undercooling $\Delta = -0.65$, and the initial radius $r = 10$.

3.1. Effect of initial radius r

We investigate the effect of the initial radius by choosing different values of $r = 10,\ 15$, and 20 in Eq. (25). The first row in Fig. 5 shows the initial states on the given sphere. The initial radii are $r = 10,\ 15$, and 20 from left to right. The second row of Fig. 5 shows the temporal evolution of the crystal growth at $t = 1200\Delta t,\ 1000\Delta t$, and $800\Delta t$ from left to right. We observe the numerical results when the size of the three crystals becomes similar. Based on this test, $r = 10$ is chosen as the initial condition for all subsequent tests.

3.2. Effect of safety scaling factor s

We consider the safety scaling factor s of the local space step h. In this case, the time step is fixed as $\Delta t = 0.025h_{min}^2$. Fig. 6 shows the sequences of the crystal growth at $t = 5000\Delta t$ with the different scaling factors $s = 0.25/\sqrt{2},\ 0.5/\sqrt{2}$, and $1/\sqrt{2}$. It is observed that a smaller scaling factor causes the crystal to grow faster. Since the safety scaling factor is related to the mesh grid size h, we choose $s = 0.5/\sqrt{2}$ for setting the mesh grid size between 0.4 and 0.8, compared with that in previous works [8,40,41].

3.3. Effect of interfacial parameter ϵ_6

To consider the effect of ϵ_6 on the sphere, the following three different values are selected: $\epsilon_6 = 0.01,\ 0.03$, and 0.05. Fig. 7(a), (b), and (c) show the crystal growth at $t = 1200\Delta t$ with $\epsilon_6 = 0.01,\ 0.03$, and 0.05, respectively. A larger ϵ_6 causes the dendrites to grow faster.

3.4. Effect of thermal diffusivity D

Next, we investigate the effect of thermal diffusivity D and fix the time step with $\Delta t = 0.1h^2/2$. Fig. 8 shows the sequences of the crystal growth at $t = 2500\Delta t$ for the different thermal diffusivity $D = 0.5,\ 1$, and 2. The results indicate that a smaller thermal diffusivity causes dendrites to grow faster.

3.5. Effect of undercooling Δ

To investigate the effect of undercooling Δ, the same test is conducted with different Δ values. Fig. 9 shows the sequences of the evolution of crystal growth at $t = 1200\Delta t$ with different undercooling $\Delta = -0.35,\ -0.45,\ -0.55$, and -0.65. It is observed that a large initial undercooling causes the dendrites to grow faster.

3.6. Growth of multiple crystals

Crystal growth on sphere is implemented by setting multiple circles as an initial condition. The initial condition is set to

$$\phi(x_p, y_p, z_p, 0) = k - 1 + \sum_{i=1}^{k} \tanh\left(\frac{r - R\theta_i}{0.01\sqrt{2}R}\right), \tag{22}$$

where k is the number of initial circles, $\theta_i = \cos^{-1}(\mathbf{N}_i \cdot \mathbf{x}_p)$ is the angle of the i-th circle for $p = 1, \dots, M$, and $\mathbf{N}_i$ is the vector from the center of the sphere to the center of the isolated circles.

Crystal growth simulations are performed for different mesh levels and different numbers of initial circles. Fig. 10(a)–(c) show the crystal growth results for level 6 mesh and five initial circles at $t = 0,\ 350$,

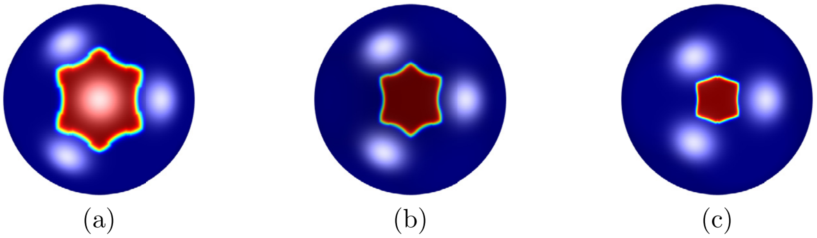
(a) (b) (c)

Fig. 6. Crystal growth on a sphere with scaling factor s at $t = 5000\Delta t$. From left to right, (a) $s = 0.25/\sqrt{2}$, (b) $s = 0.5/\sqrt{2}$, and (c) $s = 1/\sqrt{2}$.

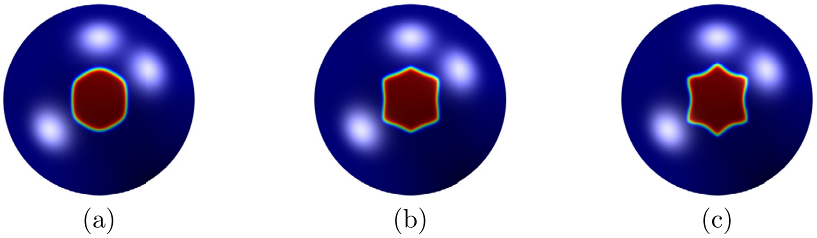
(a) (b) (c)

Fig. 7. Crystal growth on a sphere with anisotropic diffusion (a) $\epsilon_6 = 0.01$, (b) $\epsilon_6 = 0.03$, and (c) $\epsilon_6 = 0.05$.

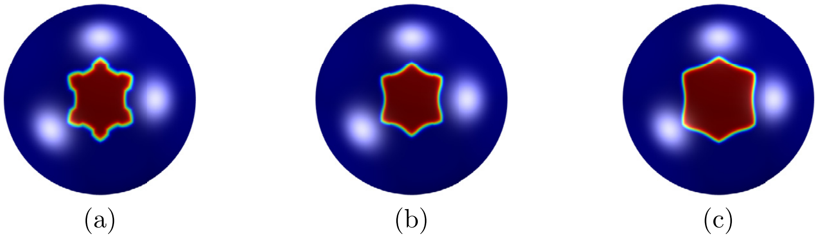
(a) (b) (c)

Fig. 8. Crystal growth on a sphere with isotropic diffusion D at $t = 2500\Delta t$. From left to right, (a) $D = 0.5$, (b) $D = 1$, and (c) $D = 2$.

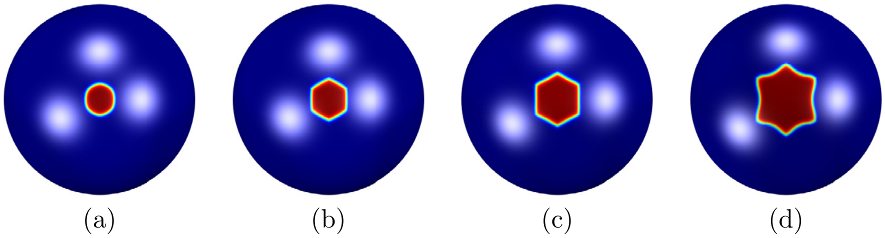
(a) (b) (c) (d)

Fig. 9. Crystal growth on a sphere with undercooling Δ at $t = 1200\Delta t$. From left to right, (a) $\Delta = -0.35$, (b) $\Delta = -0.45$, (c) $\Delta = -0.55$, and (d) $\Delta = -0.65$.

and 700, respectively. The parameters used are $r = 10$, $R = 120$, $s = 0.5/\sqrt{2}$, and the other parameters are the same as those used above. Fig. 10(d)–(f) show the crystal growth with level 7 mesh and 20 circles at $t = 600$, 1200, and 3000, respectively. The parameters used are $r = 10$, $R = 240$, $s = 0.25/\sqrt{2}$, and other parameters are the same as used above. To match the actual results in a real-world situation, five circles are added at random positions after every 200 iterations from the beginning until $t = 600$. It is observed that the interfaces of the crystals become convex inward over time.

3.7. Convergence tests

We verify the rate of convergence of the proposed method both in space and time. First, we investigate the convergence rates as the space step size h is refined. The time step size Δt is fixed to 1.0e-6 and the final time is $15\Delta t$. In addition, $r = 0.25$ and $R = 1$ are used and the other parameters are the same as described in the beginning of Section 3. The l_2-norm error between the numerical solution and the reference solution ϕ^{ref} with h is defined as $||e_h|| = \sqrt{\sum_{p=1}^{M}(\phi_p - \phi_p^{ref})^2/M}$. The numerical solution is considered with the level 8 surface mesh (i.e., $h = 0.0035$) which is a sufficiently fine mesh size for the reference solution. The rate of convergence is defined as $\log_2\left(||e_h||/||e_{h/2}||\right)$ [42].

Table 1
Rates of convergence in space.

h	0.028	Rate	0.014	Rate	0.007
l_2-norm error	3.237-3	2.143	7.328e-4	2.103	1.706e-4

Table 1 shows the l_2-norm errors and convergence rates as the space step size refines from level 5 to level 7. The proposed method is almost second-order accurate in space.

Next, the rates of convergence is examined as the time step size Δt is refined. The space step size h is fixed to 0.007 (i.e., level 7 surface mesh) and the final time 3.0e-5. The l_2-norm error with Δt is defined as $||e_{\Delta t}|| = \sqrt{\sum_{p=1}^{M}(\phi_p - \phi_p^{ref})^2/M}$. The reference solution ϕ^{ref} is considered as the numerical solution with a sufficiently small time step size $\Delta t = 3.125e\text{-}8$. The rate of convergence is defined as $\log_2\left(||e_{\Delta t}||/||e_{\Delta t/2}||\right)$.

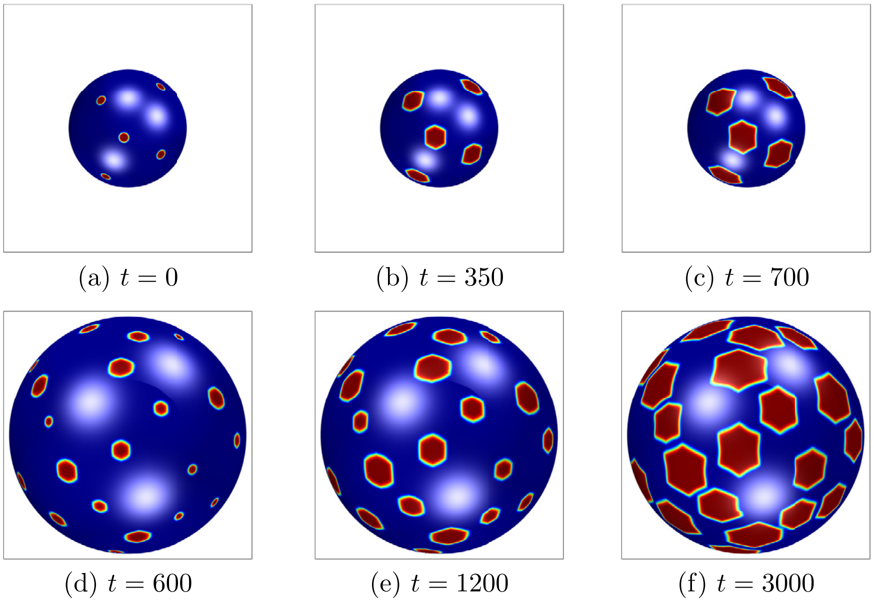
(a) $t = 0$ (b) $t = 350$ (c) $t = 700$

(d) $t = 600$ (e) $t = 1200$ (f) $t = 3000$

Fig. 10. Crystal growth on a sphere with anisotropic diffusion with (a)–(c) level 6 and (d)–(f) level 7 meshes.

Table 2
Rates of convergence in time.

Δt	1.0e-6	Rate	5.0e-7	Rate	2.5e-7
l_2-norm error	9.168e-4	1.057	4.406e-5	1.104	2.049e-5

Table 2 shows the l_2-norm errors and convergence rates as the time step size is refined. It is found that the proposed method is nearly first-order accurate in time.

From the two tables above, the accuracy of the proposed numerical method is the second-order accurate in space and the first-order accurate in time. The focus of this study is modeling for anisotropic ice crystal growth on a spherical surface. In the future work, there is a plan to develop the higher-order temporal scheme.

3.8. *Comparison of the tip velocities*

In this section, the tip velocity of the numerical solution is compared with a previous study [24] to validate the accuracy of the proposed method. Ortellado and Gómez studied crystallization on the sphere within the framework of the phase-field model and a finite difference method. However, they solved the governing equations in spherical coordinates and employed the Laplace–Beltrami operator for the diffusion term on surface. The total free energy $\mathcal{F}$ introduced in [24] is

$$\mathcal{F} = \int \left[\frac{\epsilon^2(\theta)}{2} |\nabla \phi|^2 + \frac{\phi^4}{4} - \frac{\phi^3}{2} + \frac{\phi^2}{4} + m(U) \left(\frac{\phi^3}{3} - \frac{\phi^2}{2} \right) \right] \mathrm{d}\mathbf{x},$$

where ϕ is the order parameter that is the liquid when $\phi = 0$ and the crystal phase when $\phi = 1$; U is the dimensionless temperature, $U = 0$ is the subcooling temperature, and $U_e = 1$ is the two-phase equilibrium temperature; and $m(U) = (K_1/\pi)\tan^{-1}\left(K_2(U_e - U)\right)$. Here, K_1 and K_2 are parameters such that $K_1 < 1$. The governing equation for ϕ is derived from the functional derivative of $\mathcal{F}$:

$$\frac{\partial \phi}{\partial t} = -\mu_\phi \frac{\delta F}{\delta \phi},$$

where μ_ϕ is the mobility. That is,

$$\begin{aligned} \frac{\partial \phi}{\partial t} &= \nabla \cdot (\epsilon^2(\theta)\nabla\phi) + [(\phi - 0.5) + m(U)]\, \phi(1-\phi) \\ &\quad - \left(\epsilon'(\theta)\epsilon(\theta)\phi_y\right)_x + \left(\epsilon'(\theta)\epsilon(\theta)\phi_x\right)_y . \end{aligned} \tag{23}$$

The governing equation for the temperature field U is

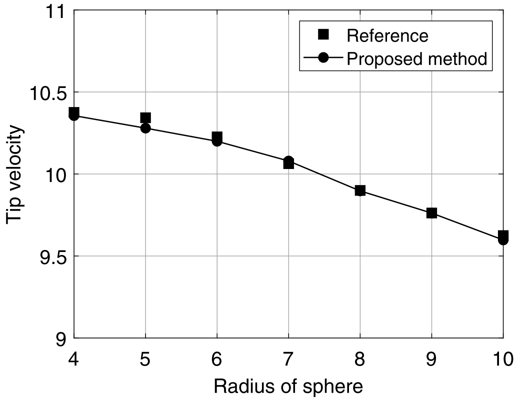

Fig. 11. Comparison of the tip velocities according to the radius of sphere.

$$\frac{\partial U}{\partial t} = \Delta U + K \frac{\partial \phi}{\partial t}, \tag{24}$$

where K is a positive constant. We compare the steady-state velocities of the tips of crystals obtained from our proposed method with the results in the reference [24]. For the comparison test, the parameters are determined as follows: the level 6 triangular surface, $K = 1$, $\epsilon_0 = \epsilon_6 = 0.029$, $K_1 = 0.9$, $K_2 = 10$, $U_0 = 1$, $\Delta t = 0.01h^2$, and the final time 0.1. The initial condition is defined as

$$\begin{aligned} \phi(x_p, y_p, z_p, 0) &= \frac{1}{2}\left[1 + \tanh\left(\frac{0.25 - R\theta}{0.01\sqrt{2}R}\right)\right], \\ U(x_p, y_p, z_p, 0) &= \phi(x_p, y_p, z_p, 0)\Delta, \end{aligned} \tag{25}$$

with $\Delta = 1$. By changing the radius R of sphere from 4 to 10, the velocities of tips is computed. Fig. 11 represents that our results for the tip velocities correspond with the reference values.

4. Discussion

The present results are important for the phase transformation processes occurring in physics, chemistry, biology, and similar research areas where the nucleation and crystal growth phenomena take place. Through the numerical results, we observed the evolution of one or multiple initial seeds and demonstrated the effects of parameters. As

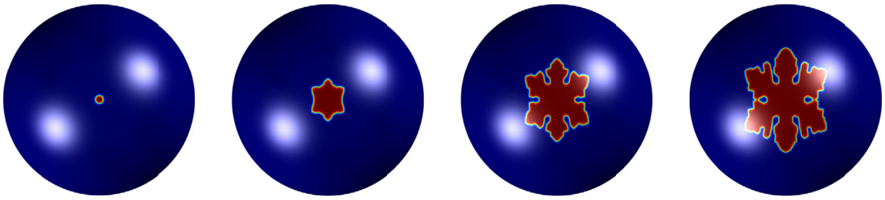

Fig. 12. Side branch formation on a sphere at $t = 0$, $9000\Delta t$, $22000\Delta t$, and $30000\Delta t$.

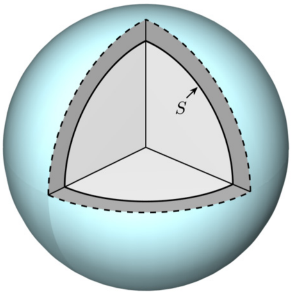

Fig. 13. Schematic of the narrow band domain on a surface S.

mentioned, it is difficult to calculate the anisotropic term on a triangular mesh of the curved surfaces in a three-dimensional space. Most of the previous studies for anisotropic ice crystal growth simulation, which are discussed in the introduction, have been performed in Cartesian coordinates, two- and three-dimensional spaces. Therefore, the novelty of the proposed method is that we presented the numerical method for implementing the anisotropic ice crystal growth on a spherical surface.

In reference [1], which motivated us to propose the current numerical method, the authors considered two conditions: isothermal and room-temperature experiments. Here, icy substrates are commonly used for the bottom. Compared to the results in [1], our results are consistent with the dynamics under the isothermal conditions. In room temperature conditions where the ambient was warmer than the melting point and freezing was accomplished with a chilled substrate, it differs from our results.

There are two limitations because this study focuses on developing the numerical method in this paper. There are two plans to improve the mathematical model and numerical method in the subsequent researches. First, we will perform the analysis and theoretical comparison in the future work. However, it is nontrivial to solve the partial differential equations on a curved surface, and it is complicated to consider the Laplace–Beltrami operator [43]. In [44,45], phase-field simulations in two-and three-dimensional geometries of ice crystal growth were presented. The complete set of non-linear equations, consisting of the undercooling balance condition and the stability criterion, were compared with phase-field simulations. Referring to those references, we will try to compare the numerical method theoretically.

Second, we need parallel computing to fully resolve the resolution. We used level 6 and 7 surface meshes that are not fine enough for the secondary branching instability of the multiple crystals. We simulate a side branch formation on the triangular surface meshes with level 8. To perform the numerical simulation for the side branching of ice crystal, the parameters are set to $\lambda = 3.1913$, $\epsilon_0 = 1$, $\epsilon_6 = 0.05$, $R = 120$, $r = 10$, $s = 0.5/\sqrt{2}$, $\Delta = -0.65$, $D = 1$, and $\Delta t = 0.1h^2/D$. Fig. 12 shows temporal evolution of the crystal growth at $t = 0$, $9000\Delta t$, $22000\Delta t$, and $30000\Delta t$ from left to right. We can observe that the side branches of the crystal. In future work, we shall present a large scale numerical results by combining our proposed method with adaptive mesh refinement or parallel computation for efficient computation [46,47].

Next, let us discuss three future potential developments. First, the present work is a two-dimensional simulation projected on a given spherical surface. It will be interesting future research if we consider the interaction between ice crystal and the lipid substrate of the bubble. Moreover, for a three-dimensional nature of crystal growth on a curved surface, we can extend the proposed method for a three-dimensional simulation on a narrow band domain [48], as shown in Fig. 13. Given surface S, we can define a narrow band domain with a small thickness, and numerically simulate a crystal growth in the domain.

Second, the proposed method can be extended to model rapid solidification of deeply supercooled ice. In high-speed solidification, a high driving force must be reached, which violates the local thermodynamic equilibrium in both the phase interface and the bulk phase, causing phase deformation [49,50]. Referring to [50], we will simulate the rapid solidification using the phase-field model numerically.

5. Conclusions

In this study, a computational technique for the phase-field model of anisotropic ice crystal growth on a spherical surface is developed. By employing the proposed numerical scheme, the terms related to the anisotropic interfacial energy can be calculated, which are difficult to compute on a triangular mesh. To resolve this problem, the governing equation was solved in Cartesian coordinates after rotating each vertex and the 1-ring neighborhood of the vertex on the triangular mesh. Various tests were conducted to demonstrate that the proposed algorithm can recover anisotropic ice crystal growth on a spherical surface.

Acknowledgement

The first author (C. Lee) was supported by the Brain Korea 21 (BK21) FOUR from the Ministry of Education of Korea. S. Yoon was supported by the National Research Foundation of Korea (NRF) grant funded by the Ministry of Science and ICT of Korea (MSIT) (No. 2019R1A6A1A11051177). H. Kim was supported by Basic Science Research Program through the National Research Foundation of Korea (NRF) funded by the Ministry of Education (NRF-2020R1A6A3A13077105). Y.B. Li is supported by National Natural Science Foundation of China (No. 11871056, No. 11631012). D. Jeong was supported by Basic Science Research Program through the National Research Foundation of Korea (NRF) funded by the Ministry of Education (NRF-2020R1F1A1A01075937). The corresponding author (J. Kim) was supported by Basic Science Research Program through the National Research Foundation of Korea (NRF) funded by the Ministry of Education (NRF-2019R1A2C1003053). The authors are grateful to the reviewers for their constructive comments on this article.

References

[1] S.F. Ahmadi, S. Nath, C.M. Kingett, P. Yue, J.B. Boreyko, How soap bubbles freeze, Nat. Commun. 10 (1) (2019) 1–10.
[2] Y. Teraoka, A. Saito, S. Okawa, Ice crystal growth in supercooled solution, Int. J. Refrig. 25 (2) (2002) 218–225.
[3] S.E. Seo, M. Girard, M.O. de la Cruz, C.A. Mirkin, Non-equilibrium anisotropic colloidal single crystal growth with DNA, Nat. Commun. 9 (1) (2018) 1–8.
[4] D.V. Alexandrov, P.K. Galenko, Dendrite growth under forced convection: analysis methods and experimental tests, Phys. Usp. 57 (8) (2014) 771.
[5] Y. Zhao, Q. Guo, T. Lin, P. Cheng, A review of recent literature on icing phenomena: transport mechanisms, their modulations and controls, Int. J. Heat Mass Transf. 159 (2020) 120074.
[6] J.S. Langer, Models of pattern formation in first-order phase transitions, in: Directions in Condensed Matter Physics, World Scientific, 1986, pp. 165–186.

[7] R. Kobayashi, Modeling and numerical simulations of dendritic crystal growth, Physica D 63 (3–4) (1993) 410–423.
[8] A. Karma, W.J. Rappel, Quantitative phase-field modeling of dendritic growth in two and three dimensions, Phys. Rev. E 57 (4) (1998) 4323.
[9] J.W. Barrett, H. Garcke, R. Nürnberg, Stable phase field approximations of anisotropic solidification, IMA J. Numer. Anal. 34 (4) (2014) 1289–1327.
[10] G. Demange, H. Zapolsky, R. Patte, M. Brunel, Growth kinetics and morphology of snowflakes in supersaturated atmosphere using a three-dimensional phase-field model, Phys. Rev. E 96 (2) (2017) 022803.
[11] G. Demange, H. Zapolsky, R. Patte, M. Brunel, A phase field model for snow crystal growth in three dimensions, npj Comput. Mater. 3 (1) (2017) 15.
[12] D.K. Sun, M.F. Zhu, S.Y. Pan, C.R. Yang, D. Raabe, Lattice Boltzmann modeling of dendritic growth in forced and natural convection, Comput. Math. Appl. 61 (12) (2011) 3585–3592.
[13] S. Meng, A. Zhang, Z. Guo, Q. Wang, Phase-field-lattice Boltzmann simulation of dendrite motion using an immersed boundary method, Comput. Mater. Sci. 184 (2020) 109784.
[14] Q. Tan, S.A. Hosseini, A. Seidel-Morgenstern, D. Thévenin, H. Lorenz, Modeling ice crystal growth using the lattice Boltzmann method, arXiv preprint, arXiv:2101.07163, 2021. (Accessed 2 August 2021).
[15] J.K. Ren, Y. Chen, Y.F. Cao, M.Y. Sun, B. Xu, D.Z. Li, Modeling motion and growth of multiple dendrites during solidification based on vector-valued phase field and two-phase flow models, J. Mater. Sci. Technol. 58 (2020) 171–187.
[16] X. Tong, C. Beckermann, A. Karma, Q. Li, Phase-field simulations of dendritic crystal growth in a forced flow, Phys. Rev. E 63 (6) (2001) 061601.
[17] S. Lee, Y. Li, J. Shin, J. Kim, Phase-field simulations of crystal growth in a two-dimensional cavity flow, Comput. Phys. Commun. 216 (2017) 84–94.
[18] Q. Li, T. Zhang, J. Yuan, Numerical simulation of polymer crystal growth under flow field using a coupled phase-field and lattice Boltzmann method, Appl. Math. Comput. 387 (2020) 124302.
[19] N. Provatas, M. Greenwood, B. Athreya, N. Goldenfeld, J. Dantzig, Multiscale modeling of solidification: phase-field methods to adaptive mesh refinement, Int. J. Mod. Phys. B 19 (31) (2005) 4525–4565.
[20] D. Jeong, J. Kim, Fast and accurate adaptive finite difference method for dendritic growth, Comput. Phys. Commun. 236 (2019) 95–103.
[21] C. Chen, X. Yang, Efficient numerical scheme for a dendritic solidification phase field model with melt convection, J. Comput. Phys. 388 (2019) 41–62.
[22] G. Meng, J. Paulose, D.R. Nelson, V.N. Manoharan, Elastic instability of a crystal growing on a curved surface, Science 343 (6171) (2014) 634–637.
[23] L. Ma, X. Liu, A.K. Soh, L. He, C. Wu, Y. Ni, Growth of curved crystals: competition between topological defect nucleation and boundary branching, Soft Matter 15 (21) (2019) 4391–4400.
[24] L. Ortellado, L.R. Gómez, Phase field modeling of dendritic growth on spherical surfaces, Front. Mater. 7 (2020) 163.
[25] S. Yoon, J. Park, J. Wang, C. Lee, J. Kim, Numerical simulation of dendritic pattern formation in an isotropic crystal growth model on curved surfaces, Symmetry 12 (7) (2020) 1155.
[26] Y. Tang, Solutions to a phase-field model of sea ice growth, Bound. Value Probl. 2019 (1) (2019) 24.
[27] A.A. Wheeler, B.T. Murray, R.J. Schaefer, Computation of dendrites using a phase field model, Physica D 66 (1–2) (1993) 243–262.
[28] Y. Li, H.G. Lee, J. Kim, A fast, robust, and accurate operator splitting method for phase-field simulations of crystal growth, J. Cryst. Growth 321 (1) (2011) 176–182.
[29] T.Z. Gong, Y. Chen, D.Z. Li, Y.F. Cao, P.X. Fu, Quantitative comparison of dendritic growth under forced flow between 2D and 3D phase-field simulation, Int. J. Heat Mass Transf. 135 (2019) 262–273.
[30] P. Jiang, S. Gao, S. Geng, C. Han, G. Mi, Multi-physics multi-scale simulation of the solidification process in the Molten pool during laser welding of aluminum alloys, Int. J. Heat Mass Transf. 161 (2020) 120316.
[31] B. Gonzalez-Ferreiro, H. Gómez, I. Romero, A thermodynamically consistent numerical method for a phase field model of solidification, Commun. Nonlinear Sci. Numer. Simul. 19 (7) (2014) 2309–2323.
[32] G. Xu, Discrete Laplace–Beltrami operators and their convergence, Comput. Aided Geom. Des. 21 (2004) 767–784.
[33] Y. Li, J. Kim, N. Wang, An unconditionally energy-stable second-order time-accurate scheme for the Cahn–Hilliard equation on surfaces, Commun. Nonlinear Sci. Numer. Simul. 53 (2017) 213–227.
[34] F. Amdjadi, Numerical simulation of reaction–diffusion equations on spherical domains, Commun. Nonlinear Sci. Numer. Simul. 13 (8) (2008) 1592–1595.
[35] S. Maddali SphereMesh, Available online, https://github.com/siddharth-maddali/SphereMesh. (Accessed 2 August 2020).
[36] X. Zhong, D. Yu, Y. San Wong, T. Sim, W.F. Lu, K.W.C. Foong, H.L. Cheng, 3D dental biometrics: alignment and matching of dental casts for human identification, Comput. Ind. 64 (9) (2013) 1355–1370.
[37] B. Chen, B. Pan, Through-thickness strain field measurement using the mirror-assisted multi-view digital image correlation, Mech. Mater. 137 (2019) 103104.
[38] D. Jeong, J. Kim, An explicit hybrid finite difference scheme for the Allen–Cahn equation, J. Comput. Appl. Math. 340 (2018) 247–255.
[39] A. Kumar, Isotropic finite-differences, J. Comput. Phys. 201 (1) (2004) 109–118.
[40] J.H. Jeong, N. Goldenfeld, J.A. Dantzig, Phase field model for three-dimensional dendritic growth with fluid flow, Phys. Rev. E 64 (4) (2001) 041602.
[41] C.C. Chen, Y.L. Tsai, C.W. Lan, Adaptive phase field simulation of dendritic crystal growth in a forced flow: 2D vs 3D morphologies, Int. J. Heat Mass Transf. 52 (5–6) (2009) 1158–1166.
[42] M. Rezaei, A.R. Yazdanian, A. Ashrafi, S.M. Mahmoudi, Numerical pricing based on fractional Black–Scholes equation with time-dependent parameters under the CEV model: double barrier options, Comput. Math. Appl. 90 (2021) 104–111.
[43] H. Kim, A. Yun, S. Yoon, C. Lee, J. Park, J. Kim, Pattern formation in reaction-diffusion systems on evolving surfaces, Comput. Math. Appl. 80 (9) (2020) 2019–2028.
[44] L.V. Toropova, P.K. Galenko, D.V. Alexandrov, M. Rettenmayr, A. Kao, G. Demange, Non-axisymmetric growth of dendrite with arbitrary symmetry in two and three dimensions: sharp interface model vs phase-field model, Eur. Phys. J. Spec. Top. 229 (19) (2020) 2899–2909.
[45] L.V. Toropova, P.K. Galenko, D.V. Alexandrov, G. Demange, A. Kao, M. Rettenmayr, Theoretical modeling of crystalline symmetry order with dendritic morphology, Eur. Phys. J. Spec. Top. 229 (2–3) (2020) 275–286.
[46] Z. Guo, S.M. Xiong, On solving the 3-D phase field equations by employing a parallel-adaptive mesh refinement (Para-AMR) algorithm, Comput. Phys. Commun. 190 (2015) 89–97.
[47] A. Zhang, J. Du, Z. Guo, Q. Wang, S. Xiong, Evolution of specific interface area during solidification: a three-dimensional thermosolutal phase-field study, Comput. Phys. Commun. 267 (2021) 108042.
[48] D. Jeong, Y. Li, C. Lee, J. Yang, J. Kim, A conservative numerical method for the Cahn–Hilliard equation with generalized mobilities on curved surfaces in three-dimensional space, Commun. Comput. Phys. 27 (2) (2020) 412–430.
[49] P.K. Galenko, V. Ankudinov, K. Reuther, M. Rettenmayr, A. Salhoumi, E.V. Kharanzhevskiy, Thermodynamics of rapid solidification and crystal growth kinetics in glass-forming alloys, Philos. Trans. R. Soc. A 377 (2143) (2019) 20180205.
[50] P.K. Galenko, D. Jou, Rapid solidification as non-ergodic phenomenon, Phys. Rep. 818 (2019) 1–70.